Journal of Materials Chemistry C

PAPER

Cite this: J. Mater. Chem. C, 2017, 5, 6973

Facet-engineered CeO_2/graphene composites for enhanced NO_2 gas-sensing†

Lizhai Zhang, ‡[a] Qinglong Fang,‡[a] Yuhong Huang,[b] Kewei Xu,*[ac] Fei Ma*[a] and Paul K. Chu*[d]

Received 8th April 2017,
Accepted 18th June 2017

DOI: 10.1039/c7tc01523b

rsc.li/materials-c

The sensitivity of semiconductor gas sensors depends on the exposed crystal planes. High-energy crystal planes usually have an open surface structure and more active sites which favor the absorption of gas molecules and thus might improve the gas sensing performance. However, it is commonly difficult for the high-energy crystal planes to be exposed. In this paper, the morphology and exposed facets of CeO_2 nanoparticles in the CeO_2 nanoparticles/graphene composites are tailored simply by changing the volume ratio of ethylene glycol to deionized water (EG/H_2O) in the solution during fabrication. CeO_2 nanocubes enclosed by the {100} facets are produced with an EG/H_2O ratio of 1 : 1, otherwise CeO_2 nanograins enclosed by the {111} facets are obtained, which is closely related to the changes in the energetics on the surface. Furthermore, it is found that the CeO_2{100}/graphene composites deliver substantially enhanced gas sensing performance for NO_2, as compared to CeO_2{111}/graphene composites. First-principles calculations illustrate that the electrons flow from graphene to the CeO_2{111} facets resulting in electron depletion on graphene. In contrast, the electrons flow from the CeO_2{100} surface to graphene resulting in electron accumulation on graphene and the band gap of CeO_2{100}/graphene is nearly zero implying a metallic behavior. The rapid charge exchange between NO_2 and CeO_2{100}/graphene composites leads to the improved gas sensing properties. The results present us a clear physical picture for the tunable facets and morphology as well as the enhanced performances of nanoparticles/graphene composites.

1. Introduction

Nitrogen dioxide (NO_2) is one of the common and toxic air pollutants from combustion and automotive emission causing serious diseases such as chronic bronchitis, emphysema, and respiratory irritation.[1–3] Therefore, it is crucial to develop high-performance sensors to detect NO_2 in air quickly and reliably. Many sensing devices including metal oxide semiconductor gas sensors, solid electrolyte gas sensors, optic fiber gas sensors, and surface acoustic wave (SAW) gas sensors have been developed[4–7] and among them, metal oxide semiconductors have attracted much attention. However, they normally operate at a high temperature resulting in high power consumption[8] and so low-cost, high-sensitivity, and fast-response sensing materials are much more desirable especially in portable devices.

Essentially, the gas sensing performance of metal oxides is mainly restricted by the lower electrical conductivity at room temperature.[9] To solve this problem, the composites of metal oxides and another material with high electrical conductivity could be developed. As well known, graphene possesses a large specific surface area, high electrical conductance,[10] low signal-to-noise level, and stable response to NO_2 at room temperature.[11–14] If metal oxide nanoparticles can be uniformly dispersed on graphene sheets, the electrical conductance and the charge exchange between metal oxide and NO_2 can be significantly improved, and the structure is expected to have excellent gas sensing characteristics.[9] The composites combining graphene with SnO_2, ZnO, WO_3, Co_3O_4, and Cu_2O have been shown to deliver good sensing performance for NO_2 at room temperature.[15–19]

Compared to other metal oxides, CeO_2 has more active gas sensing properties due to its polymorphism and mixed valence,

[a] State Key Laboratory for Mechanical Behavior of Materials, Xi'an Jiaotong University, Xi'an 710049, Shaanxi, China. E-mail: mafei@mail.xjtu.edu.cn
[b] College of Physics and Information Technology, Shaanxi Normal University, Xi'an 710062, Shaanxi, China
[c] Department of Physics and Opt-electronic Engineering, Xi'an University of Arts and Science, Xi'an 710065, Shaanxi, China. E-mail: kwxu@mail.xjtu.edu.cn
[d] Department of Physics and Materials Science, City University of Hong Kong, Tat Chee Avenue, Kowloon, Hong Kong, China. E-mail: paul.chu@cityu.edu.hk

† Electronic supplementary information (ESI) available: Elemental maps of the CeO_2/graphene nanocomposite; the surface energy of CeO_2{111} and {100} planes as well as the adsorption energy of ethylene glycol; the work function of the CeO_2{111} plane, graphene, the CeO_2{100} plane terminated with Ce and the CeO_2{100} plane terminated with O; the energy band configurations of CeO_2{111} and graphene composites; the DOS and PDOS of the CeO_2{111} plane and the CeO_2{100}–Ce plane. See DOI: 10.1039/c7tc01523b

‡ Dual contributors.

and it becomes one of the potential candidate materials in the field of gas sensing.[20] Fu *et al.* successfully synthesized the composites of CeO_2 nanoparticles and graphene, and illustrated their fast response to 100 ppm NO_2, but the sensitivity is only 10.39% at room temperature.[20] It is mandatory to improve the sensitivity through modification of CeO_2 nanoparticles. Since gas sensing is a surface process, the sensitivity depends on the exposed crystal planes.[21–23] Usually, high-energy crystal planes have an open surface structure and more active sites[24–29] which favor the absorption of gas molecules. Furthermore, the electronic states are also facet dependent and hence, the energy band alignment of the heterojunction and charge transfer across the interface in composites may be adjusted by changing the facets of metal oxides.[30] Accordingly, the gas sensing performance of CeO_2/graphene composites might be enhanced by controllable faceting of CeO_2 nanoparticles. As for CeO_2, the {100} plane is an open surface and should exhibit more active properties than {111} and {110} planes.[31–36] However, the surface energy of the CeO_2{100} plane is higher and the atomic configuration is less stable than the {111} and {110} facets.[37] Consequently, CeO_2{100} planes diminish rapidly during grain growth[38] and synthesis of CeO_2 with controllable facets is still challenging.

In this work, the hydrothermal method is adopted to fabricate the composites of CeO_2 nanoparticles and graphene, and it is found that the morphology and facets of the CeO_2 nanoparticles in the composites can be tailored simply by changing the volume ratio of ethylene glycol (EG) to deionized water (H_2O) in the solution. Compared to CeO_2{111} facets/graphene composites, CeO_2{100} facets/graphene composites exhibit higher sensitivity and more rapid response to NO_2. In particular, the sensitivity to 100 ppm NO_2 is 33% at room temperature, and it is enhanced by 200% as compared to the reported results (10.39%).[20] It is demonstrated that the gas sensing performance of CeO_2/graphene composites could be enhanced by controllable faceting of CeO_2 nanoparticles. First-principles calculations are performed to elucidate the mechanisms for the controllable faceting as well as the enhanced performance.

2. Experimental and theoretical section

2.1 Material preparation

Graphene oxide (GO) was synthesized from pure graphite powders by the modified Hummers method[39] and graphene was prepared by reduction of GO with H_2 at 400 °C for 1 h. 10 mg of graphene were dissolved in a solvent consisting of ethylene glycol (EG) and deionized water (H_2O) with different volume ratios (EG + H_2O = 0 mL + 40 mL, 10 mL + 30 mL, 20 mL + 20 mL, 30 mL + 10 mL, or 40 mL + 0 mL) under sonication for 2 h. 0.5 mmol $Ce(NO_3)_3{\cdot}6H_2O$, 1.5 mmol NaOH, and 0.3 g of PVP were added to the solvent and stirred magnetically for 3 h. The mixture was transferred to a 100 mL Teflon-lined autoclave and heated to 180 °C for 24 h. Afterwards, the precipitate was washed three times with distilled water and ethanol and dried at 70 °C in a vacuum oven overnight to obtain the CeO_2/graphene nanocomposite. Pure CeO_2 nanoparticles were prepared in the same manner at different EG/H_2O volume ratios (0 : 40, 10 : 30, 20 : 20, 30 : 10, and 40 : 0), respectively.

2.2 Characterization

The X-ray diffraction (XRD) patterns were acquired between 10° and 90° (SHIMADZU XRD-7000S) with Cu K_α radiation. Raman spectra were recorded on a Horiba HR800 spectrometer with a 633 nm laser as the excitation source. The morphology of the samples was characterized using scanning electron microscopy (SEM, FEI Quanta 600S) and high-resolution transmission electron microscopy (HR-TEM, JEOL JEM 2100F). The Mott–Schottky curves were measured on an electrochemical analyzer (CHI760E, Shanghai). The voltage in the Mott–Schottky measurement was scanned from −0.4 V to 0.4 V *versus* SCE (saturated calomel reference electrode) at a frequency of 10 000 Hz and 0.5 M $NaSO_2$ was used as the electrolyte. A Keithley 4200 Semiconductor Characterization System was used to obtain the current–voltage (*I–V*) curves.

2.3 Gas sensing measurements

5 mg of CeO_2/graphene powder were dispersed in 1 mL of ethyl alcohol under sonication for 30 min and then 0.2 mL of the suspension was added dropwise onto SiO_2 with interdigitated gold electrode arrays with a pipette. The substrate was heated to 60 °C for 15 min to evaporate the solvent before the gas sensing measurement. The sensor was installed in a test chamber with an inlet and an outlet. The electrical resistance was measured at room temperature at a relative humidity (RH) of 26%. The gas concentration was controlled by injection and the chamber was purged with air to recover the resistance.

2.4 Theoretical model and calculations

Density-functional theory (DFT) calculations were conducted using the Vienna ab initio simulation package (VASP).[40–42] The kinetic energy cutoff for the plane wave basis set was 500 eV. Brillouin zone integration on grids with 3 × 3 × 1 and 11 × 11 × 1 Monkhorst–Pack *k*-points was implemented for geometrical optimization and calculation of the density of states, respectively. Geometrical optimization was performed by using the conjugate gradient scheme until the Hellman–Feynman force was smaller than 0.05 eV $Å^{-1}$. The vacuum space perpendicular to the CeO_2/graphene is around 15 Å, which was enough to separate the interaction between periodic images. To model the interface, a 2 × 2 CeO_2(111) slab (O–Ce–O, nine layers) and a 3 × 3 graphene sheet were stacked with a lattice mismatch of 3.7%, while a 2 × 2 CeO_2(100) slab (eight layers), and a 3 × 2 graphene sheet were stacked with a lattice mismatch of 4.6%. A 3 × 3 slab was employed to calculate the surface energy and adsorption energy. The slab thickness was 10 Å and the vacuum space between the slabs was 20 Å. The surface energy was calculated using the following equation:

$$E = \frac{E_{surf} - nE_{bulk}}{A} \quad (1)$$

in which E_{surf} is the total energy of the slab, E_{bulk} is the average energy of each CeO_2 unit in the bulk, and n is the number of CeO_2 units in each slab. The surface area of the slab is denoted by A.

The absorption energy of ethylene glycol on the CeO_2 nanoparticles was calculated as follows:

$$E_{ads} = E_{(EG+CeO_2)} - E_{EG} - E_{CeO_2} \quad (2)$$

where E_{EG+CeO_2} is the total energy of the relaxed ethylene glycol–CeO_2 system, E_{EG} is the energy of free ethylene glycol, and E_{CeO_2} is the total energy of the relaxed CeO_2 slab.

The formation energy of the CeO_2/graphene hybrid structure was calculated as:

$$E = E_{CeO_2/graphene} - E_{CeO_2} - E_{graphene} \quad (3)$$

in which $E_{CeO_2/graphene}$ is the total energy of the relaxed CeO_2/graphene system, E_{CeO_2} is the total energy of the relaxed CeO_2 slab, and $E_{graphene}$ is the total energy of the relaxed graphene slab.

3. Results and discussion

3.1 Characterization of CeO_2/graphene composites

The synthesis process is schematically illustrated in Fig. 1 and the detailed experimental procedures are described in the Experimental section. The CeO_2/graphene nanocomposites are characterized by XRD, Raman spectra, SEM, TEM, and HR-TEM. As shown in Fig. 2, the main XRD peaks can be assigned to the (111), (200), (220), (311), (222), (400), (331), (420) and (422) planes of CeO_2 in a cubic fluorite-type structure (a = 5.41 Å, $Fm\bar{3}m$ space group, JCPDS card no. 34-394). The XRD peaks from CeO_2 decrease gradually from samples (a) to (e) and the full width at half-maximum (FWHM) increases gradually due to suppressed growth of the CeO_2 nanoparticles with the introduction of ethylene glycol. According to Scherrer's equation, the average size of the CeO_2 nanoparticles is about

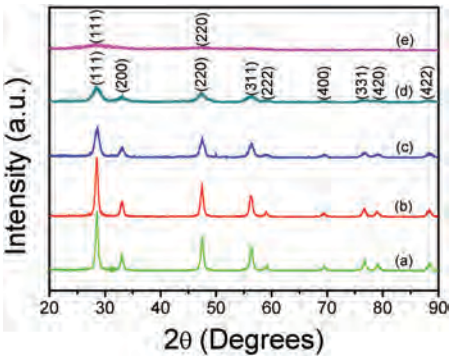

Fig. 2 XRD patterns of the CeO_2/graphene composites prepared with different EG/H_2O volume ratios: (a) 0 : 40, (b) 10 : 30, (c) 20 : 20, (d) 30 : 10, and (e) 40 : 0.

20 nm, 15 nm, 10 nm, and 5 nm for samples (a) to (d), respectively. Fig. 3 shows the Raman spectra of graphene, CeO_2, and CeO_2/graphene composites. Two prominent peaks corresponding to the G and D bands of graphene are observed. The G band is usually assigned to the E_{2g} vibration mode and the D band is associated with structural defects with the A_{1g} symmetry.[43,44] The intensity ratios of D to G bands (I_D/I_G) are 1.03, 1.13, 1.06, 1.05, and 1.04 for samples (a) to (e), respectively, which are larger than that of graphene (0.97) due to partial modification of the functional groups and formation of new sp^2 clusters during reduction.[45] The new peak at 463 cm^{-1} from CeO_2/graphene composites corresponds to symmetrical stretching of the Ce–O bond, and is sensitive to the structural disorder in the oxygen sub-lattice.[46] The peak red-shifts from 465 cm^{-1} in CeO_2 to 463 cm^{-1} in CeO_2/graphene composites as a result of charge transfer between them.

The morphology of the CeO_2/graphene nanocomposites is characterized by SEM, TEM and HR-TEM, and the results are shown in Fig. S1 (ESI†) and Fig. 4. As shown in Fig. S1 (ESI†), CeO_2 nanoparticles are dispersedly attached on graphene

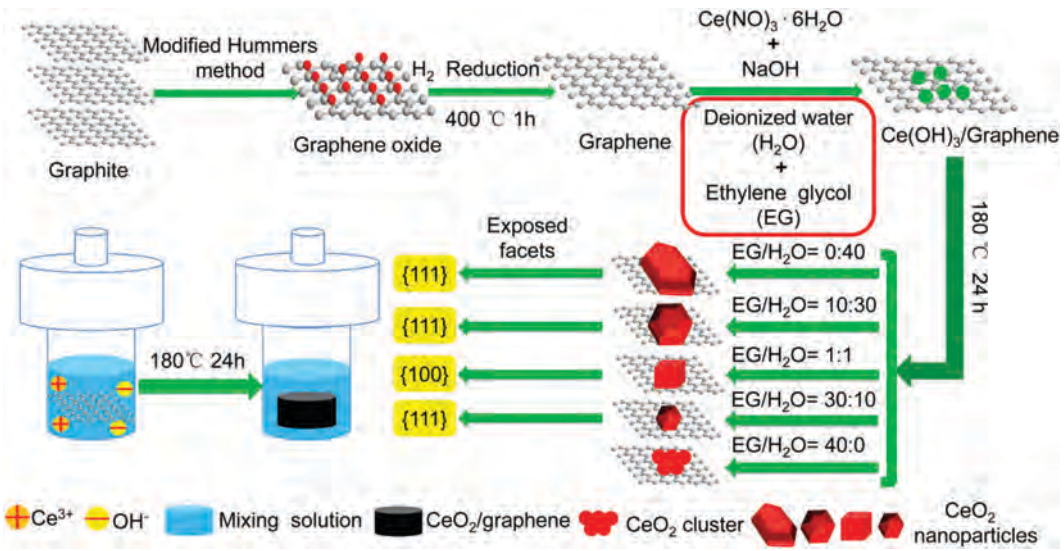

Fig. 1 Schematic illustration of the synthesis of CeO_2/graphene composites.

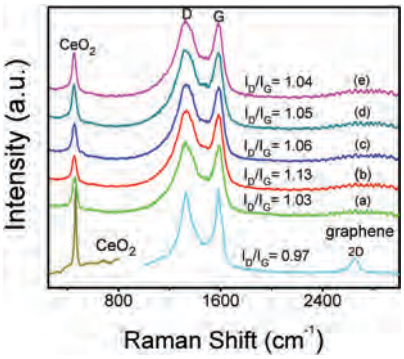

Fig. 3 Raman spectra of the CeO_2, graphene and CeO_2/graphene nanocomposites prepared with different EG/H_2O volume ratios: (a) 0 : 40, (b) 10 : 30, (c) 20 : 20, (d) 30 : 10, and (e) 40 : 0.

sheets, and almost no isolated CeO_2 nanoparticles are evidenced. Since the graphene sheets were synthesized by reduction of graphene oxide, there are commonly a great number of oxygen groups, vacancies and other structural defects.[9] As a result, the nucleation and growth of CeO_2 nanoparticles are preferred on graphene sheets because of the strong interaction between them. This leads to good adhesion between CeO_2 nanoparticles and graphene sheets. Fig. 4 shows the SEM, TEM and HR-TEM images of the CeO_2/graphene nanocomposites prepared with different EG/H_2O volume ratios. If deionized water (40 mL H_2O) is used, the CeO_2 nanocrystals have an irregular octahedral shape with an average diameter of 20 nm (Fig. 4a_1 and a_2).

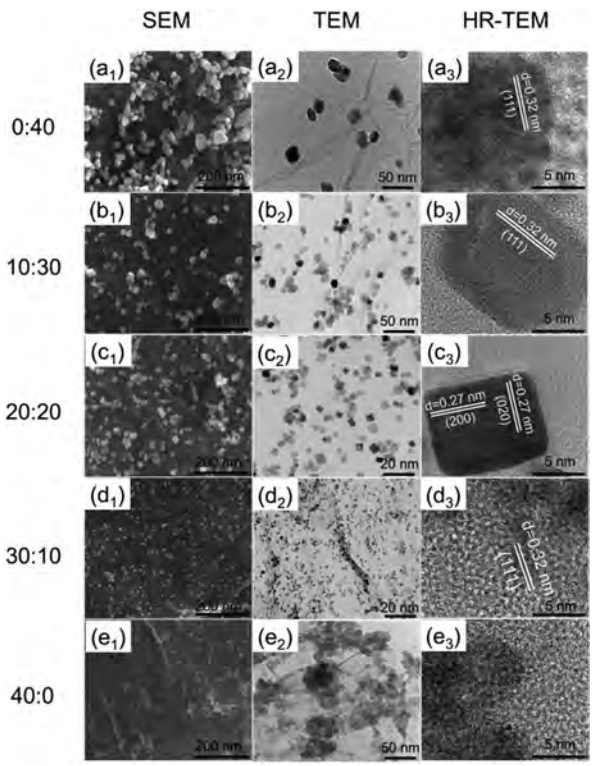

Fig. 4 SEM, TEM and HR-TEM images of the CeO_2/graphene nanocomposites prepared with different EG/H_2O volume ratios: (a) 0 : 40, (b) 10 : 30, (c) 20 : 20, (d) 30 : 10, and (e) 40 : 0.

Clear lattice fringes with a separation of 0.32 nm observed from the side surface correspond to the {111} facets of CeO_2 (Fig. 4a_3). When the volume ratio of EG/H_2O is increased to 10 : 30, the CeO_2 nanoparticles evolve into an irregular truncated octahedral morphology with an average size of 15 nm (Fig. 4b_1 and b_2) and they are also mainly enclosed by the {111} facets (Fig. 4b_3). When the volume ratio of EG/H_2O is further adjusted to 20 : 20, CeO_2 nanoparticles become nanocubes with an average size of 10 nm (Fig. 4c_1 and c_2). As shown in the HR-TEM image in Fig. 4c_3, the lattice spacing perpendicular to the sides of cubes is 0.27 nm corresponding to the {200} planes of CeO_2. This means that CeO_2 nanocubes enclosed by the {200} planes are synthesized. If the volume ratio of EG/H_2O is increased to 30 : 10, the CeO_2 becomes irregular truncated octahedrons again but with a reduced size of 5 nm (Fig. 4d_1 and d_2) and the CeO_2 nanocrystals are enclosed by the {111} facets (Fig. 4d_3). If the EG/H_2O volume ratio is increased to 40 : 0, that is, only EG in the solution, CeO_2 nanoclusters in lieu of nanoparticles are obtained (Fig. 4e_1–e_3). If the volume ratio of EG/H_2O is changed to 10 : 10, 15 : 15, or 25 : 25 (that is, the same volume of EG and H_2O), the cubic morphology of the CeO_2 particles enclosed by {100} facets is maintained (Fig. 5). The EDS maps in Fig. S2 (ESI†) show that C, O, and Ce are homogeneously distributed throughout the samples confirming the formation of the CeO_2/graphene composite.

3.2 The role of EG in controlling the facets and morphology of CeO_2 nanoparticles

In order to understand the role of ethylene glycol in the formation of the CeO_2{111} and {100} facets, density functional theory (DFT) calculations are performed to determine the surface energy of the {111} and {100} facets as well as the absorption energy of ethylene glycol. Fig. S3 (ESI†) presents the results. The surface energy of the {100} facets (5.1 J m^{-2}) is higher than that of the {111} facets (0.70 J m^{-2}) by 600%. Growth on the {100} facets is more rapid and so the {100} facets disappear gradually resulting in the formation of irregular octahedral CeO_2 nanoparticles

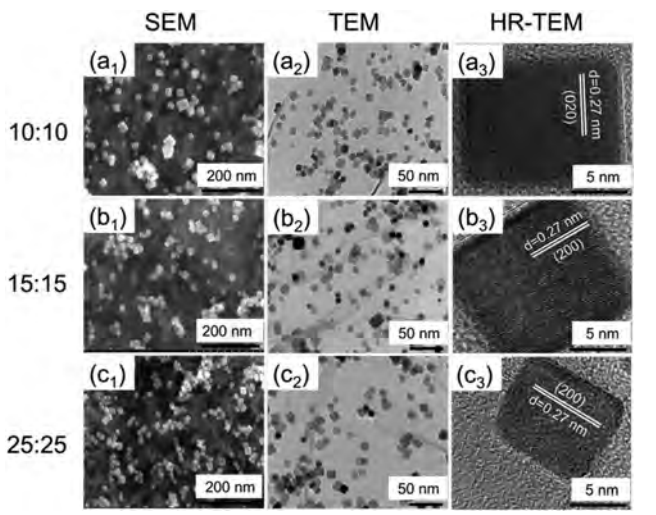

Fig. 5 SEM, TEM and HR-TEM images of the CeO_2/graphene nanocomposites prepared with different EG/H_2O volume ratios: (a) 10 : 10, (b) 15 : 15, and (c) 25 : 25.

with the {111} facets being exposed (Fig. 4a$_1$–a$_3$). Furthermore, the absolute value of adsorption energy for each ethylene glycol molecule on the {100} facets (0.7 eV) is larger than that on the {111} facets (0.047 eV). Hence, the ethylene glycol molecules preferentially absorb on the {100} facets and the surface energy of the {100} facets decreases from 5.1 J m^{-2} to −1.43 J m^{-2}, which is even smaller than that of the clean {111} facets (0.7 J m^{-2}). Consequently, the growth on the {111} facets becomes more rapid, and CeO_2 nanoparticles surrounded by the {100} facets are fabricated by using the appropriate volume ratio of EG/H_2O (for instance, 20 : 20) in the hydrothermal process. This promotes the formation of nanocubes with {100} facets exposed (Fig. 4c$_1$–c$_3$). However, adsorption of EG on the {111} facets becomes strong at large concentrations of ethylene glycol. Growth on all facets is then suppressed and the surface energy of the {111} facets (−9.71 J m^{-2}) becomes the smallest again giving rise to the formation of small CeO_2 nanoparticles surrounded by the {111} facets (Fig. 4d$_1$–d$_3$). At a sufficiently large concentration of ethylene glycol, for example, at a volume ratio of EG/H_2O of 40 : 0, there are enough ethylene glycol molecules absorbed on the facets and growth on all exposed facets is inhibited leading to nano-clusters (Fig. 4e$_1$–e$_3$). So the concentration of ethylene glycol is crucial to control the exposed facets as well as the morphology and size of the CeO_2 nanoparticles.

3.3 The gas sensing performances of CeO_2/graphene composites

Fig. 6 displays the Mott–Schottky (MS) curves. They are approximately linear with a negative slope for both CeO_2 nanoparticles and CeO_2/graphene composites, indicative of p-type semiconducting behaviour. The carrier density can be calculated by the Mott–Schottky equation:

$$\frac{1}{C_{SC}{}^2} = \frac{2}{e\varepsilon\varepsilon_0 N}\left(E - E_{fb} - \frac{KT}{e}\right) \quad (4)$$

where C_{SC} is the capacitance of the space charge region, e is the electronic charge, ε is the relative dielectric constant of the CeO_2, ε_0 is the permittivity under vacuum, N is the hole density, E is the applied potential, E_{fb} is the flat band potential, K is the Boltzmann constant, and T is the absolute temperature.[47] The densities of holes in the CeO_2 nanoparticles with exposed {111} facets, CeO_2/{111} facets/graphene composites, CeO_2 nanoparticles with exposed {100} facets, and CeO_2/{100} facets/graphene composites were about 1.18 × 10^{19} cm^{-3}, 2.87 × 10^{19} cm^{-3}, 3.37 × 10^{19} cm^{-3} and 7.67 × 10^{19} cm^{-3}, respectively. Hence, the carrier concentration is increased by 100% in the CeO_2/graphene nanocomposites.

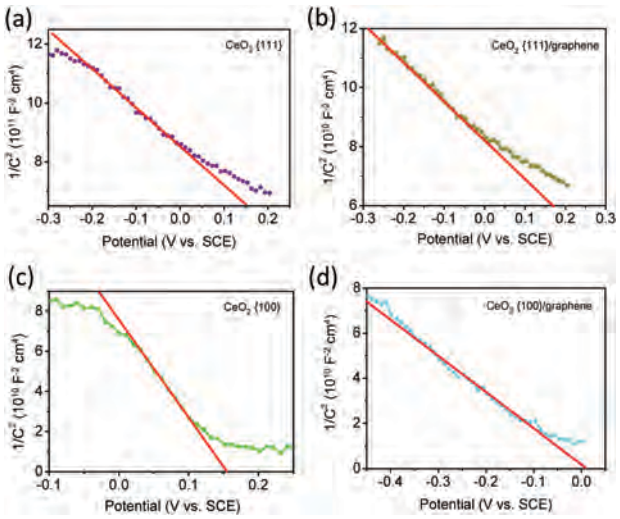

Fig. 6 Mott–Schottky plots of the CeO_2{111} plane, CeO_2{100} plane, CeO_2{111}/graphene and CeO_2{100}/graphene nanocomposites.

The sensitivity of the samples to NO_2, $(R_{gas} - R_{air})/R_{air}$, is determined, in which R_{gas} and R_{air} denote the resistance of the sample exposed to NO_2 gas and air, respectively. First of all, the response curves of the CeO_2/graphene sensor were measured at different temperatures, and the results are shown in Fig. S4 (ESI†). As the working temperature is increased, the response and recovery times are shortened, but the sensitivity is greatly lowered. At room temperature, adsorption of NO_2 continues during the gas exposure, while desorption is negligible owing to the strong bonding between NO_2 and CeO_2/graphene nanocomposites.[48] Prior to the equilibrium between adsorption and desorption, the sensor resistance decreases continuously with increasing NO_2 coverage.[48] However, the desorption of NO_2 is enhanced at higher working temperature, the balance between adsorption and desorption in both gas exposure and recovering process can be quickly reached.[48] So the response and recovery times are shortened at higher working temperatures, and the sensitivity is lowered. The better room-temperature sensing performance of CeO_2/graphene nanocomposites is expected for monitoring inflammable and explosive environments.[49] Fig. 7a shows a sensitivity of 50 ppm NO_2 at room temperature. During exposure to NO_2, the resistance of CeO_2/graphene nanocomposites decreases sharply. NO_2 is an electron acceptor due to the unpaired electrons on the nitrogen atoms.[48] The electrons will transfer from CeO_2/graphene composites to NO_2 thereby increasing the concentration of holes in CeO_2/graphene composites and reducing the electrical resistance. During subsequent exposure to air, NO_2 molecules desorb from the surface and the resistance goes up.[48] The sensitivity values of the samples a–e are 9.88%, 10.57%, 24.82%, 17.78%, and 7.76%, respectively, being 1.79, 1.92, 4.51, 3.23, and 1.41 times that of pure CeO_2 nanoparticles (5.50%). In particular, sample c with CeO_2 nano-cubes surrounded by the {100} facets delivers the best sensing performance. The sensitivity is enhanced by 350% and the response and recovery times by which 90% of the resistance is restored in the adsorption and desorption processes are about 30 s and 85 s, respectively (Fig. 7b). As shown in Fig. 7c, the sensitivity of pure CeO_2 and CeO_2/graphene composites decreases with NO_2 concentrations in the range from 200 ppm to 10 ppm. Sample c with CeO_2 nano-cubes surrounded by the {100} facets always shows the highest sensitivity and 10 ppm NO_2 gas can be detected with a large resistance variation of 14%. It is enhanced by 1400% and 140% compared to pure CeO_2 nanoparticles and CeO_2{111} facets/graphene composites (sample d), respectively. Fig. 7d shows the response time to NO_2 in the concentration range of 10–200 ppm. The response time decreases with increasing concentrations of NO_2 and in particular, from 75 s

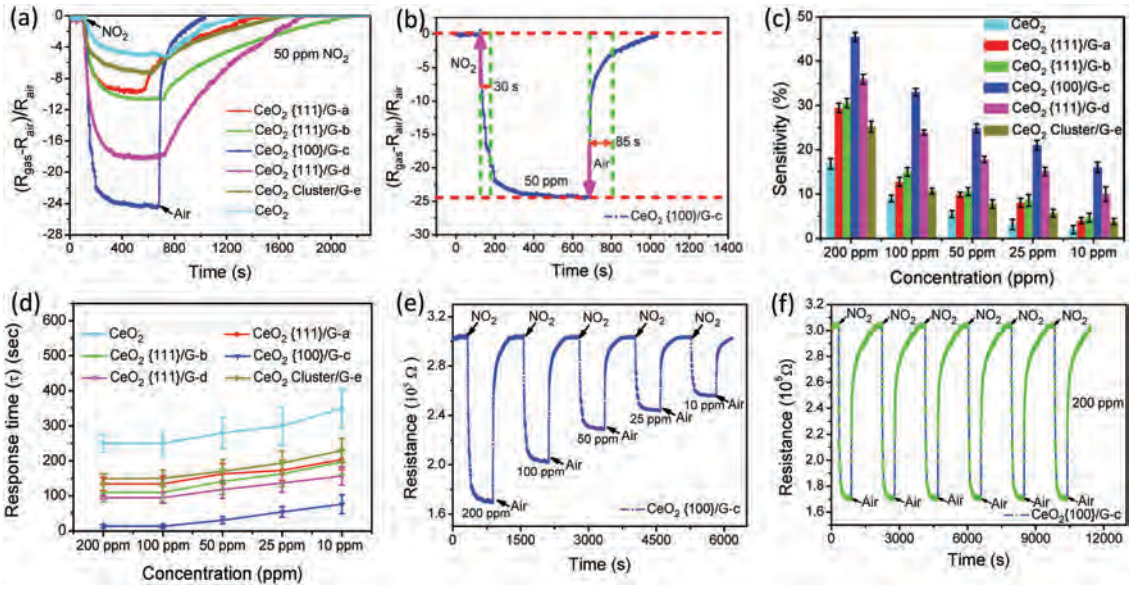

Fig. 7 (a) Resistance variation of CeO_2, CeO_2/graphene composites a–e with respect to 50 ppm NO_2; (b) response and recovery curves of CeO_2/graphene-c in the presence of 50 ppm NO_2 gas at room temperature; (c) sensitivity of pure CeO_2, CeO_2/graphene composites a–e for 10–200 ppm NO_2 at room temperature; (d) response time to 10–200 ppm NO_2. (e) Response and recovery curves of CeO_2{100}/graphene-c for 10–200 ppm NO_2 at room temperature; (f) electrical resistance of CeO_2/graphene-c *versus* time in the presence of 200 ppm NO_2. (G: graphene)

to 15 s for sample c (CeO_2{100}/graphene composites). It means that the NO_2 molecules are more tightly bound on the CeO_2{100} surface than on the CeO_2{111} surface. As for CeO_2{111} facets/graphene composites, the sensing performance decreases in the following order: sample d > sample b > sample a, indicating that smaller CeO_2 nano-particles increase the sensitivity of CeO_2/graphene composites. Fig. 7e and Fig. S5 (ESI†) show the response and recovery curves of CeO_2{100}/graphene (sample c) and CeO_2{111}/graphene sensors (sample a, b, d, and e) to NO_2 gas of different concentrations at room temperature, respectively. Clearly, the resistance of the CeO_2{100}/graphene sensor decreases quickly during exposure to NO_2 but reverts to the initial value fast upon exposure to air, indicating good response and recovery performance. Fig. 7f shows six response cycles of sample c during exposure to 200 ppm NO_2. The cycling curves nearly coincide with each other demonstrating stable sensing. The long-term stability of the sensor was evaluated through exposure to 200 ppm NO_2 for a period of ten days. As shown in Fig. S6 (ESI†), the sensor exhibits good stability and the error is smaller than 5%.

Selectivity is also an important parameter for gas sensors. The responses of the CeO_2{100}/graphene composites to NO_2, NH_3, and O_2 have been measured. The results are shown in Fig. S7 (ESI†), and the responses to NO_2, O_2, NH_3, H_2, CO, and C_2H_2 reported by others[20] are also summarized for comparison. It is clearly that the CeO_2{100}/graphene composites exhibit the highest sensitivity to NO_2 among them, and thus an excellent selectivity toward NO_2 at room temperature.

3.4 Gas-sensing mechanism

The gas-sensing properties of metal oxides are mainly dependent on the exposed facets.[50] As shown in Fig. S8 (ESI†), the exposed {100} polar facets are the real reason for the good sensing performance of CeO_2 nanoparticles to NO_2 gas at room temperature. Structurally, each Ce atom is eightfold-coordinated with O atoms and each O atom is fourfold-coordinated with Ce atoms in the bulk, but they are unsaturated on the surface. Each O or Ce atom on the CeO_2{111} surface has one dangling bond and two on the {100} surface. Therefore, there are more dangling bonds on the {100} surface than on the {111} surface.[51] Consequently, the {100} facet is more active in adsorbing NO_2 at room temperature. What is more, the {100} polar surface usually contains more oxygen vacancies than {111} nonpolar facets.[51] The oxygen vacancies can significantly enhance the adsorption of oxygen molecules, and electrons will transfer from the oxygen vacancies in CeO_2 to the oxygen molecules, resulting in more oxygen species (especially O_2^-). These oxygen species will react with NO_2, resulting in a more abrupt change in the conductivity of the sensor.[52] The graphene sheets in the composites improve the electrical conductivity of CeO_2 and thus the gas sensing performance at room temperature substantially.[9] Furthermore, the overlapped and crumpled regions on graphene sheets provide a large surface area, thus facilitate the effective access of gases onto CeO_2/graphene composites.[53] Finally, a strong electronic interaction occurs at the interface of graphene and CeO_2, which will modulate the charge exchange during gas-sensing,[54] which is further confirmed using first-principles calculations.

3.5 Effect of facets on gas sensing performance

Fig. 8a and Fig. S9 (ESI†) show the work functions of the CeO_2{111} plane, the CeO_2{100} plane terminated with cerium (CeO_2{100}–Ce), the CeO_2{100} plane terminated with oxygen (CeO_2{100}–O), and graphene, respectively. The work function of the CeO_2{111} facet (6.14 eV) is larger than that of graphene (4.54 eV) and the electrons will transfer from graphene to the

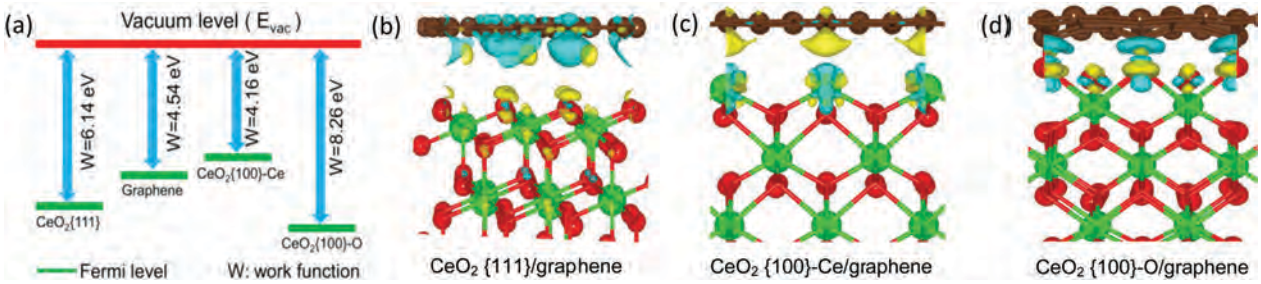

Fig. 8 (a) The work function of the CeO_2{111}, graphene, CeO_2{100}–Ce, and CeO_2{100}–O plane; 3D charge density differences of (b) CeO_2{111}/graphene hybrid structure, (c) CeO_2{100}–Ce/graphene hybrid structure and (d) CeO_2{100}–O/graphene hybrid structure. Yellow and cyan represent electron accumulation and depletion, respectively. The C, Ce, and O atoms are represented by brown, green and red balls, respectively.

CeO_2{111} facet, resulting in electron depletion on graphene and electron accumulation on the CeO_2{111} plane, as evidenced from the 3D charge density difference in Fig. 8b. The energy bands of CeO_2{111} planes are bent down and hole depletion occurs at the interface (Fig. S10, ESI†). This leads to Schottky contact. Structurally, the CeO_2{100} plane can be either oxygen or cerium terminated.[51] The formation energy of the hybrid structure of graphene and the CeO_2{100}–Ce plane (−5.14 eV) is lower than that with O termination (−4.39 eV), and the CeO_2{100}–Ce/graphene hybrid structure is the stable one. Because the Fermi level of the CeO_2{100}–Ce plane is higher than that of graphene (Fig. 8a), the electrons are transferred from the CeO_2{100}–Ce surface to graphene, leading to electron depletion on the CeO_2{100}–Ce plane and electron accumulation on graphene, as confirmed by the 3D charge density difference in Fig. 8c. The polarity of the CeO_2{100}–Ce surface is compensated to some degree and the CeO_2{100}–Ce surface becomes more stable, which is different from the previously reported results.[55,56] Supposing that the CeO_2{100} plane is oxygen terminated, the Fermi level will be much lower than that of graphene (Fig. 8a), and the electrons will be transferred from graphene to CeO_2{100} (Fig. 8d), resulting in Schottky contact. This is not consistent with the measured *I–V* curves (Fig. 10). So the heterogeneous interface of graphene and the CeO_2{100}–Ce plane is preferential.

To gain more insights into their electronic origin, the total and projected density of states of the CeO_2{111} plane, the CeO_2{100}–Ce plane, CeO_2{111} facets/graphene composites, and CeO_2{100}–Ce facets/graphene composites are calculated based on DFT. As shown in Fig. S11a and b (ESI†), the valence band maximum (VBM) and the conduction band minimum (CBM) of the CeO_2{111} plane are dominated by the O 2p and Ce 4f states, respectively. The Fermi level is close to the VBM (O 2p) characteristic of a p-type semiconductor and in agreement with the *M–S* curve. The VBM and CBM of the CeO_2{100}–Ce facets are dominated by the O 2p and Ce 4f states, respectively and overlapped at the Fermi level, suggesting a metallic behavior (Fig. S11c and d, ESI†). When the hetero-interface is formed between graphene and the CeO_2{111} plane, the VBM and the CBM are mainly determined by the C 2p and Ce 4f states, respectively (Fig. 9a and b). The band gap between the occupied C 2p state and the unoccupied Ce 4f state is about 0.4 eV, which is larger than the thermal energy at room temperature (0.026 eV). Therefore, it is difficult for the electrons

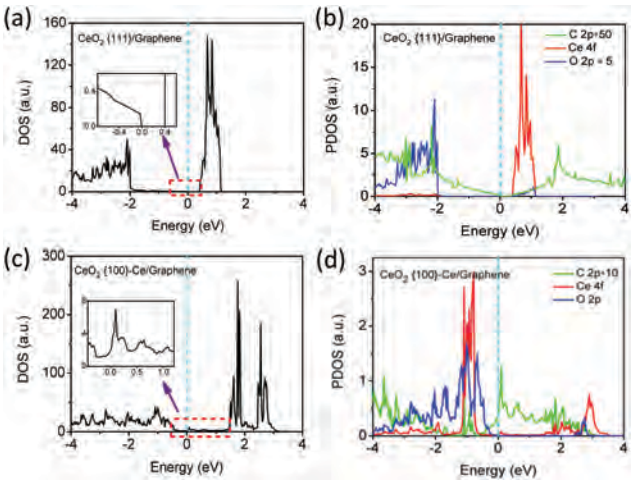

Fig. 9 The DOS and PDOS of (a and b) CeO_2{111}/graphene and (c and d) CeO_2{100}–Ce/graphene composites, respectively. The dashed lines indicate the Fermi level.

to transfer from the VBM of graphene to the CBM of CeO_2{111} at room temperature. However, as shown in Fig. 9c and d, the VBM and CBM of the CeO_2{100}–Ce/graphene hetero-interface are determined by the O 2p and C 2p states, respectively, and they overlap at the Fermi level, suggesting a metallic behavior. It is easy for the electrons to transfer from the VBM of the CeO_2{100} plane to the CBM of graphene at room temperature. Owing to their high carrier mobility in graphene, rapid charge exchange takes place between NO_2 and CeO_2{100} facets/graphene composites. Consequently, the sensitivity, response and recovery are enhanced.

The current *versus* voltage (*I–V*) curves of the CeO_2 nanoparticles, graphene sheets, CeO_2{111} facets/graphene composites, and CeO_2{100}–Ce facets/graphene composites are shown in Fig. 10. The slope of CeO_2/graphene composites is larger than that of pure CeO_2 nanoparticles as a result of reduced resistance. The *I–V* curve of CeO_2{111} facets/graphene composites is non-linear, revealing the Schottky contact, but that of CeO_2{100}–Ce facets/graphene composites is linear, suggesting the Ohmic contact. This confirms the above theoretical prediction, and the hybrid structures of graphene and CeO_2 nanocubes surrounded by the {100} facets are crucial to the enhanced NO_2 sensing performance.

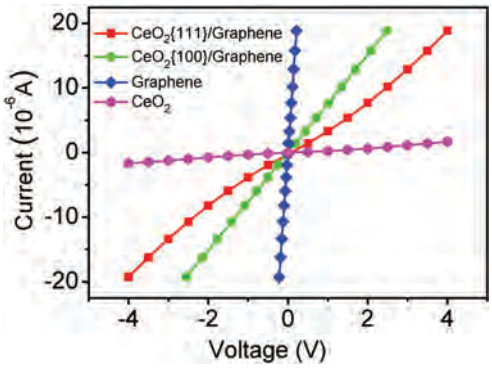

Fig. 10 $C-V$ curves of CeO_2 nanoparticles, graphene sheets, CeO_2{111}/graphene, and CeO_2{100}/graphene nanocomposites.

4. Conclusion

The hydrothermal method is adopted to fabricate CeO_2/graphene nanocomposites. It is found that the shape and facets of the CeO_2 nanocrystals can be adjusted simply by changing the volume ratio of ethylene glycol to deionized water in the solution. When the volume ratio of ethylene glycol to deionized water is 1 : 1, cubic CeO_2 nanoparticles surrounded by high-energy {100} facets are obtained, otherwise CeO_2 nanograins enclosed by the {111} facets are obtained, which is closely related to the changes in the energetics on surface. As compared to CeO_2{111}/graphene composites, the CeO_2{100}/graphene nanocomposites exhibit an excellent response to NO_2, for example, the sensitivity during exposure to 10 ppm NO_2 is increased by 1400% as compared to pure CeO_2. First-principles calculations reveal that electrons transfer from graphene sheets to the CeO_2{111} planes producing electron depletion on graphene at the interface. In contrast, the electrons move from the CeO_2{100} planes to graphene sheets and, the VBM and the CBM overlap at the Fermi level producing a metallic behavior. Therefore, NO_2 can easily capture electrons from the CeO_2{100} facets/graphene nanocomposites at room temperature and the sensitivity of NO_2 detection is significantly enhanced. The results present us a clear physical picture for the tunable facets and morphology as well as the enhanced performances of metal oxide nanoparticles/graphene composites.

Acknowledgements

This work was jointly supported by the National Natural Science Foundation of China (Grant No. 51471130), Natural Science Foundation of Shaanxi Province (No. 2017JZ015), Fundamental Research Funds for the Central Universities, and the City University of Hong Kong Applied Research Grant (ARG) No. 9667122.

References

1 J. Kong, N. R. Franklin, C. Zhou, M. G. Chapline, S. Peng, K. Cho and H. J. Dai, *Science*, 2000, **287**, 622.
2 G. Ko, H. Y. Kim, J. Ahn, Y. M. Park, K. Y. Lee and J. Kim, *Curr. Appl. Phys.*, 2010, **10**, 1002.
3 "Nitrogen Dioxide," Environmental Protection Agency, http://www.epa.gov/airquality/nitrogenoxides/, accessed: Feb. 2015.
4 N. D. Chinh, N. V. Toan, V. V. Quang, N. V. Duy, N. D. Hoa and N. V. Hieu, *Sens. Actuators, B*, 2014, **201**, 7.
5 C. Zamani, K. Shimanoe and N. Yamazoe, *Sens. Actuators, B*, 2005, **109**, 216.
6 S. I. Ohira, P. K. Dasgupta and K. A. Schug, *Anal. Chem.*, 2009, **81**, 4183.
7 C. Wen, C. Zhu, Y. Ju, H. Xu and Y. Qiu, *Sens. Actuators, A*, 2010, **159**, 168.
8 Z. Y. Wang, Y. Zhang, S. Liu and T. Zhang, *Sens. Actuators, B*, 2016, **222**, 893.
9 W. J. Yuan and G. Q. Shi, *J. Mater. Chem. A*, 2013, **1**, 10078.
10 X. Du, I. Skachko, A. Barker and E. Y. Andrei, *Nat. Nanotechnol.*, 2008, **3**, 491.
11 F. Schedin, A. K. Geim, S. V. Morozov, E. W. Hill, P. Blake, M. I. Katsnelson and K. S. Novoselov, *Nat. Mater.*, 2007, **6**, 652.
12 A. K. Geim and K. S. Novoselov, *Nat. Mater.*, 2007, **6**, 183.
13 K. S. Novoselov, D. Jiang, F. Schedin, T. J. Booth, V. V. Khotkevich, S. V. Morozov and A. K. Geim, *Proc. Natl. Acad. Sci. U. S. A.*, 2005, **102**, 10451.
14 J. D. Fowler, M. J. Allen, V. C. Tung, Y. Yang, R. B. Kaner and B. H. Weiller, *ACS Nano*, 2009, **3**, 301.
15 Z. Y. Wang, Y. Zhang, S. Liu and T. Zhang, *Sens. Actuators, B*, 2016, **222**, 893.
16 S. Liu, B. Yu, H. Zhang, T. Fei and T. Zhang, *Sens. Actuators, B*, 2014, **202**, 272.
17 P. G. Su and S. L. Peng, *Talanta*, 2015, **132**, 398.
18 N. Chen, X. Li, X. Wang, J. Yu, J. Wang, Z. Tang and S. A. Akbarb, *Sens. Actuators, B*, 2013, **188**, 902.
19 S. Deng, V. Tjoa, H. Fan, H. Tan, D. C. Sayle, M. Olivo, S. Mhaisalkar, J. Wei and C. H. Sow, *J. Am. Chem. Soc.*, 2012, **134**, 4905.
20 Y. Yang, C. G. Tian, L. Sun, R. J. Lv, W. Zhou, K. Y. Shi, K. Kan, J. C. Wang and H. G. Fu, *J. Mater. Chem. A*, 2013, **1**, 12742.
21 M. Batzill, *Sensors*, 2006, **6**, 1345.
22 M. Batzill, K. Katsiev, J. M. Burst, U. Diebold, A. M. Chaka and B. Delley, *Phys. Rev. B: Condens. Matter Mater. Phys.*, 2005, **72**, 165414.
23 J. D. Prades, A. Cirera and A. J. R. Morante, *J. Electrochem. Soc.*, 2007, **154**, 675.
24 N. Tian, Z. Y. Zhou, S. G. Sun, Y. Ding and Z. L. Wang, *Science*, 2007, **316**, 732.
25 N. Tian, Z. Y. Zhou and S. G. Sun, *J. Phys. Chem. C*, 2008, **112**, 19801.
26 Z. Y. Zhou, Z. Z. Huang, D. J. Chen, Q. Wang, N. Tian and S. G. Sun, *Angew. Chem., Int. Ed.*, 2010, **49**, 411.
27 X. W. Xie, Y. Li, Z. Q. Liu, M. Haruta and W. J. Shen, *Nature*, 2009, **458**, 746.
28 L. H. Hu, Q. Peng and Y. D. Li, *J. Am. Chem. Soc.*, 2008, **130**, 16136.
29 X. G. Han, H. Z. He, Q. Kuang, X. Zhou, X. H. Zhang, T. Xu, Z. X. Xie and L. S. Zheng, *J. Phys. Chem. C*, 2009, **113**, 584.
30 H. F. Li, H. T. Yu, X. Quan, S. Chen and H. M. Zhao, *Adv. Funct. Mater.*, 2015, **25**, 3074.

31 E. Aneggi, J. Llorca, M. Boaro and A. Trovarelli, *J. Catal.*, 2005, **234**, 88.
32 K. Zhou, X. Wang, X. Sun, Q. Peng and Y. Li, *J. Catal.*, 2005, **229**, 206.
33 H. X. Mai, L. D. Sun, Y. W. Zhang, R. Si, W. Feng, H. P. Zhang, H. C. Liu and C. Y. Yan, *J. Phys. Chem. B*, 2005, **109**, 24380.
34 D. C. Sayle, S. A. Maicaneanu and G. W. Watson, *J. Am. Chem. Soc.*, 2002, **124**, 11429.
35 G. S. Herman, *Surf. Sci.*, 1999, **437**, 207.
36 N. V. Skorodumova, M. Baudin and K. Hermansson, *Phys. Rev. B: Condens. Matter Mater. Phys.*, 2004, **69**, 075401.
37 P. W. Tasker, *J. Phys. C: Solid State Phys.*, 1979, **12**, 4977.
38 G. Liu, J. C. Yu, G. Q. Lu and H. M. Cheng, *Chem. Commun.*, 2011, **47**, 6763.
39 D. C. Marcano, D. V. Kosynkin, J. M. Berlin, A. Sinitskii, Z. Z. Sun, A. Slesarev, L. B. Alemany, W. Lu and J. M. Tour, *ACS Nano*, 2010, **4**, 4806.
40 G. Kresse and J. Furthmüller, *Phys. Rev. B: Condens. Matter Mater. Phys.*, 1996, **54**, 11169.
41 G. Kresse and J. Hafner, *Phys. Rev. B: Condens. Matter Mater. Phys.*, 1993, **48**, 13115.
42 G. Kres and D. Joubert, *Phys. Rev. B: Condens. Matter Mater. Phys.*, 1999, **59**, 1758.
43 K. Krishnamoorthy, M. Veerapandian, R. Mohan and S. J. Kim, *Appl. Phys. A: Mater. Sci. Process.*, 2012, **106**, 501.
44 D. X. Yang, A. Velamakanni, G. Bozoklu, S. Park, M. Stoller, R. D. Piner, S. Stankovich, J. Inhwa, D. A. Field, C. A. Ventrice Jr and R. S. Ruoff, *Carbon*, 2009, **47**, 145.
45 J. F. Che, L. Y. Shen and Y. H. Xiao, *J. Mater. Chem.*, 2010, **20**, 1722.
46 I. Kosacki, T. Suzuki, V. Petrovsky, H. U. Anderson and P. Colomban, *Solid State Ionics*, 2002, **149**, 99.
47 W. W. Zhang, H. L. Guo, H. Q. Sun and R. C. Zeng, *Appl. Surf. Sci.*, 2016, **382**, 128.
48 H. Long, A. H. Trochimczyk, T. Pham, Z. R. Tang, T. L. Shi, A. Zettl, C. Carraro, M. A. Worsley and R. Maboudian, *Adv. Funct. Mater.*, 2016, **26**, 5158.
49 W. Yang, P. Wan, X. D. Zhou, J. M. Hu, Y. F. Guan and L. Feng, *ACS Appl. Mater. Interfaces*, 2014, **6**, 21093.
50 A. Gurlo, *Nanoscale*, 2011, **3**, 154.
51 W. X. Huang and Y. X. Gao, *Catal. Sci. Technol.*, 2014, **4**, 3772.
52 S. Q. Tian, F. Yang, D. W. Zeng and C. S. Xie, *J. Phys. Chem. C*, 2012, **116**, 10586.
53 A. Tricoli, M. Righettoni and A. Teleki, *Angew. Chem., Int. Ed.*, 2010, **49**, 7632.
54 J. Zhang, X. H. Liu, G. Neri and N. Pinna, *Adv. Mater.*, 2016, **28**, 795.
55 G. S. Herman, *Phys. Rev. B: Condens. Matter Mater. Phys.*, 1999, **59**, 14899.
56 O. Stetsovych, J. Beran, F. Dvorák, K. Masek, J. Myslivecek and V. Matolín, *Appl. Surf. Sci.*, 2013, **285**, 766.